

VFM-Recon: Unlocking Cross-Domain Scene-Level Neural Reconstruction with Scale-Aligned Foundation Priors

Yuhang Ming^{1,2*}, Tingkang Xi^{2*}, Xingrui Yang^{3*}, Lixin Yang¹,
Yong Peng^{2†}, Cewu Lu¹, and Wanzeng Kong²

¹ Shanghai Jiao Tong University, Shanghai, China

² Hangzhou Dianzi University, Hangzhou, China

³ CARDC, Mianyang, China

{yuhang.ming, tingkangxi, yongpeng, kongwanzeng}@hdu.edu.cn

yangxingrui@cardc.cn {siriusyang, lucewu}@sjtu.edu.cn

* Equal contribution, †Corresponding author.

Abstract. Scene-level neural volumetric reconstruction from monocular videos remains challenging, especially under severe domain shifts. Although recent advances in vision foundation models (VFMs) provide transferable generalized priors learned from large-scale data, their scale-ambiguous predictions are incompatible with the scale consistency required by volumetric fusion. To address this gap, we present **VFM-Recon**, *the first attempt* to bridge transferable VFM priors with scale-consistent requirements in scene-level neural reconstruction. Specifically, we first introduce a lightweight scale alignment stage that restores multi-view scale coherence. We then integrate pretrained VFM features into the neural volumetric reconstruction pipeline via lightweight task-specific adapters, which are trained for reconstruction while preserving the cross-domain robustness of pretrained representations. We train our model on ScanNet train split and evaluate on both in-distribution ScanNet test split and out-of-distribution TUM RGB-D and Tanks and Temples datasets. The results demonstrate that our model achieves state-of-the-art performance across all datasets domains. In particular, on the challenging outdoor Tanks and Temples dataset, our model achieves an F1 score of *70.1* in reconstructed mesh evaluation, substantially outperforming the closest competitor, VGGT, which only attains *51.8*.

Keywords: Neural Reconstruction · Visual Foundation Models · Cross-Domain Generalization · Scale Alignment

1 Introduction

Scene-level 3D volumetric reconstruction from monocular RGB video aims to construct a unified geometric representation of an entire scene that is globally consistent across all views. It is a fundamental problem in computer vision, supporting applications such as robotic navigation, mixed reality interactions, and

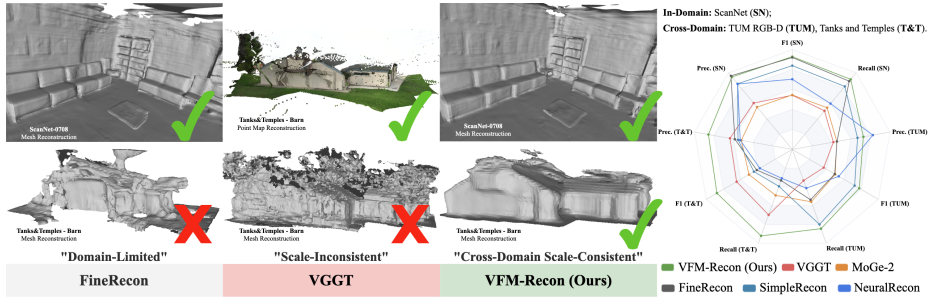


Fig. 1: We present **VFM-Recon**, a novel framework that enables cross-domain, scale-consistent neural volumetric reconstruction. Existing neural reconstruction methods such as FineRecon [32] perform well on indoor scenes but struggles under domain shift, while VFMs such as VGGT [38] predicts plausible point maps, yet lack scale consistency for mesh reconstruction. The radar plot highlights consistent performance gains across ScanNet [6], TUM RGB-D [35], and Tanks and Temples [18].

digital twin modeling. Classical approaches build such representations through a depth-estimation-and-fusion paradigm [28, 50]. While theoretically grounded, these geometry-driven methods depend heavily on sufficient view overlap and robust feature matching.

To overcome these limitations, recent learning-based approaches replace explicit multi-view stereo with learned feature aggregation and volumetric decoding, enabling temporally coherent reconstruction from RGB video [27, 32, 36]. By implicitly aggregating multi-view cues within convolutional encoders and volumetric decoders, these methods achieve strong performance on indoor benchmarks [6]. However, unlike classical approaches that explicitly enforce geometric constraints, neural volumetric reconstruction systems primarily rely on learned scene priors [32]. Their performance is therefore tightly coupled to the training distribution and degrades under domain shifts, such as transferring from indoor to outdoor environments, as shown in Figure 1.

In parallel, vision foundation models (VFMs), pretrained on large-scale data, demonstrate robust cross-domain generalization across diverse tasks [38, 49]. Recent analyses reveal that these models encode structured geometric priors [21], and their representations can enhance downstream 3D reasoning systems [20, 55]. For neural reconstruction, VFMs provide two complementary signals: explicit geometric predictions such as monocular depth, and transferable geometry-aware feature embeddings that can strengthen multi-view aggregation. It is worth noting that unlike recent large reconstruction models [1, 13, 54] that focus on object-level reconstruction, we are, to the best of our knowledge, the first to systematically leverage VFM priors to enhance scene-level neural volumetric reconstruction under domain shifts.

Yet directly injecting VFM priors into volumetric reconstruction is non-trivial. Although VFM-predicted depth captures strong relative structure, it remains scale-ambiguous and may exhibit inter-frame inconsistency over long

sequences [25, 53]. In contrast, volumetric fusion requires scale consistent multi-view observations [16, 32]; even small scale mismatches accumulate during fusion, leading to unstable geometry, as shown in Figure 1. This exposes a structural incompatibility: VFMs provide transferable geometric priors without scale guarantees, whereas volumetric reconstruction critically depends on scale-consistent integration.

In this work, we propose a novel framework that reconciles VFM priors with scale-consistent neural volumetric reconstruction through a decoupled design. We introduce a *lightweight scale alignment stage* that resolves global and local scale ambiguity in VFM depth using relative camera poses and pairwise geometric consistency. Rather than re-optimizing trajectories or dense volumes, we estimate a compact set of scale factors to restore multi-view coherence, enabling stable volumetric fusion. Then, in the *VFM-augmented volumetric reconstruction stage*, we integrate task-adapted VFM feature embeddings into the volumetric reconstruction network. These features act as geometry-aware structural priors, improving cross-domain robustness while preserving the scale stability required for consistent scene-level fusion, as shown in Figure 1.

To validate our design, we conduct extensive experiments on ScanNet [6] using the official train/test splits. To evaluate cross-domain generalization, we further test on out-of-distribution indoor scenes from TUM RGB-D [35] and challenging outdoor scenes from Tanks and Temples [18]. Our model achieves state-of-the-art (SoTA) performance across all domains.

In summary, our contributions are threefold:

1. We are, to the best of our knowledge, **the first** to systematically leverage VFM priors to enhance **scene-level neural volumetric reconstruction** under domain shifts, bridging transferable foundation representations with scale-consistent fusion requirements.
2. We propose a **lightweight scale alignment module** that resolves global and local scale ambiguity using geometric consistency without requiring full scene re-optimization.
3. We introduce a **VFM-augmented volumetric reconstruction network** that significantly improves cross-domain generalization while maintaining reconstruction quality within the training domain.

2 Related Work

2.1 Neural Volumetric Reconstruction

Neural volumetric reconstruction departs from classical depth-fusion pipelines by directly regressing scene-level geometry from posed RGB images. Atlas [27] first demonstrated end-to-end signed distance function (SDF) prediction via feature back-projection and 3D convolution, establishing the direct volumetric regression paradigm. Subsequent works improved scalability and multi-view reasoning over video streams: NeuralRecon [36] introduced sequential SDF prediction with recurrent fusion, while VoRTX [34] and TransformerFusion [2] adopted transformer-based global attention for more expressive multi-view integration.

As multi-view fusion matured, surface detail preservation became central challenges. SimpleRecon [30] emphasized strong multi-view depth priors with lightweight fusion, whereas FineRecon [32] introduced resolution-agnostic supervision and depth-guided refinement for sharper surfaces. DG-Recon [16] and CVRecon [12] addressed ray-wise feature redundancy and empty-space ambiguity via geometry- and cost-volume-guided fusion. More recent works [4, 5, 42, 58] further focus on adaptive feature modeling, hierarchical alignment, and sparsification strategies to preserve fine structures while maintaining efficiency.

Beyond fidelity improvements, recent trends explore structured representations and feedback-driven mechanisms to enhance scene-level reasoning and efficiency. Plane-centric neural representations have been proposed to enforce compactness and semantic alignment within volumetric pipelines [31, 43, 51]. Double-Take [29] feeds reconstructed geometry back into depth estimation to stabilize inference, while semantic-oriented methods [15, 46, 56] incorporate higher-level reasoning into volumetric pipelines. GP-Recon [57] integrates explicit geometric priors with online optimization for fine-grained detail preservation, and Ani-Grad [33] reduces surface extraction cost via adaptive sampling guided by local surface complexity.

2.2 Geometry-Aware Foundation Models

More recently, VFMs pretrained on large-scale data have increasingly been applied to geometry-centric tasks, including monocular depth estimation, multi-view geometry, and monocular 3D reconstruction.

In monocular depth estimation, DepthCues [8] analyzes the emergence of depth perception in pretrained vision models. Metric3D [14, 52] addresses metric ambiguity through canonical camera modeling for zero-shot metric depth generalization, while the MoGe series [39, 40] extends prediction to affine- and metric-scale 3D point maps with improved structural detail. The Depth Anything series [22, 48, 49] demonstrates that scaling data, model capacity, and distillation strategies enhances cross-domain robustness and spatial consistency.

For multi-view geometry, pretraining strategies increasingly encode cross-view spatial reasoning. CroCo [44, 45] introduces cross-view masked modeling to learn transferable geometry-aware representations. DUST3R [41] proposes direct pointmap regression from image pairs without explicit calibration, unifying monocular and binocular reconstruction in a feed-forward manner. MAST3R and its extensions [10, 19, 26] enhance matching accuracy and integrate learned priors into SfM and SLAM systems. MUST3R [3] generalizes pairwise prediction to symmetric multi-view reconstruction with improved scalability, while VGGT and VGGT-SLAM [25, 38] extend feed-forward geometry engines to jointly infer camera parameters, point maps, and globally consistent alignment.

3 Methodology

Given a RGB image sequence $\mathcal{I} = \{I_t\}_{t=1}^N$ with known camera poses $\mathcal{T} = \{\mathbf{T}_t \in SE(3)\}_{t=1}^N$ and intrinsics $\mathbf{K} \in \mathbb{R}^{3 \times 3}$, our goal is to reconstruct a dense scene-

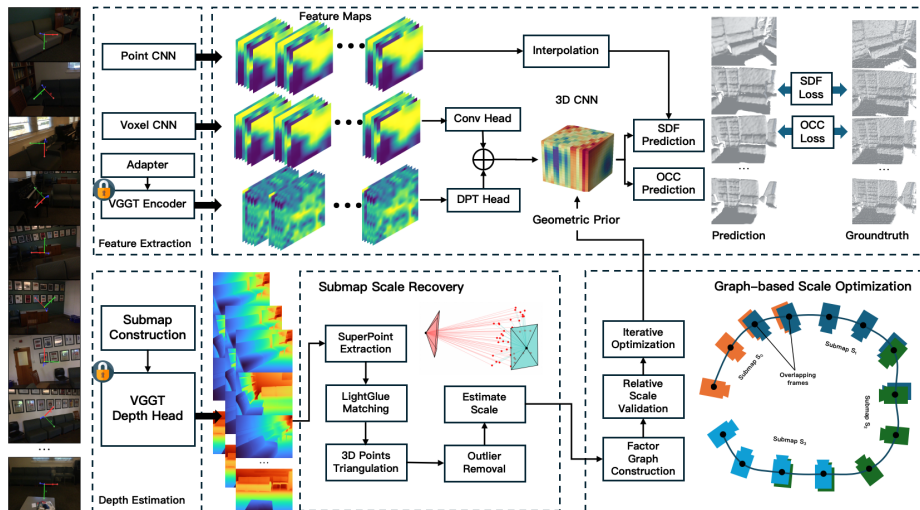


Fig. 2: System Overview. On the top is our *VFM-augmented volumetric reconstruction network*, and in the bottom is our *lightweight scale alignment module*. Our system divides the sequence into overlapping submaps and uses VGGT [38] to predict scale-ambiguous depths. It then recovers per-submap scales via feature matching and triangulation, followed by factor-graph global scale optimization. The aligned depth are further refined with a fuse-and-back-projection process and are used as geometric priors for subsequent VFM-augmented neural reconstruction.

level SDF volume \mathcal{V} from which we extract a mesh \mathcal{M} via iso-surface extraction. To manage computational complexity while maintaining geometric coverage, we first subsample a sparse set of *keyframes* $\mathcal{I}' = \{I_{k_1}, I_{k_2}, \dots, I_{k_P}\} \subset \mathcal{I}$ from the original sequence using the strategy proposed in [11], and perform all subsequent stages on \mathcal{I}' . An overview of the our system is given in Figure 2.

3.1 Aligning Foundation Model Priors

We leverage the depth maps predicted by VGGT [38] as dense geometric priors from the keyframes. Within a single inference batch, the predicted depths are typically coherent up to a shared *relative* scale, yielding geometrically plausible structure. However, VGGT is not trained with strict metric supervision, so its depth predictions are only defined up to an unknown *sequence-dependent* scale. As a result, VGGT depths cannot be directly fused with camera poses with different scales (e.g., from SLAM/SfM), motivating a scale alignment stage that restores multi-view consistency.

Submap Selection Strategy We divide the selected keyframes \mathcal{I}' into M overlapping submaps $\{\mathcal{S}_m\}_{m=1}^M$. Each submap contains n consecutive keyframes, and adjacent submaps overlap by o frames: $\mathcal{S}_m = \{I_{k_t}\}_{t=(m-1)(n-o)+1}^{\min((m-1)(n-o)+n, P)}$. Compared to submap designs that share only a few views [50], our construction

preserves a larger overlap to support more reliable scale constraints between neighboring submaps.

For each submap \mathcal{S}_m , we run VGGT independently and obtain depth predictions $\{\hat{D}_{k_t}^m\}_{k_t \in \mathcal{S}_m}$. Within a submap, the predicted depths exhibit consistent relative scale, producing geometrically coherent depth maps that capture fine geometric details. However, each submap’s predictions are defined up to an unknown scale factor $\sigma_m \in \mathbb{R}_{>0}$ specific to that submap, which leads to scale-ambiguity.

Per-submap Scale Recovery To recover global scale for each submap without needing a prior global map, we employ feature matching and triangulation. For each submap \mathcal{S}_m , we find correspondences between overlapping frames using SuperPoint [9] and LightGlue [24]. Given camera poses \mathbf{T}_t and feature correspondences, we triangulate 3D points and verify each triangulation through reprojection error checks and Chirality tests. Only points satisfying both constraints, i.e., positive depth along the optical axis and reprojection error below a threshold, are retained. These filtered 3D points provide globally consistent depth values z_t^p at pixels \mathbf{u}_t^p . For each submap, we compute an initial scale factor by taking the robust median ratio between triangulated depths and the network predictions:

$$s_m^{(0)} = \operatorname{median}_p \left\{ \frac{z_t^p}{\hat{D}_t^m(\mathbf{u}_t^p)} \right\}. \quad (1)$$

Graph-Based Scale Optimization While the per-submap scales recovery provide initial alignment, scale inconsistencies remain across submaps due to noisy triangulation and outlier contamination. To achieve globally consistent scale factors, we formulate a graph optimization problem over submap scales.

For each adjacent submap pair $(\mathcal{S}_i, \mathcal{S}_{i+1})$ with overlapping keyframes, we compare the VGGT depths predicted for the *same* overlapping frames when they appear in different submaps. For an overlapping keyframe t , let \hat{D}_t^i and \hat{D}_t^{i+1} denote the predicted depths from submaps \mathcal{S}_i and \mathcal{S}_{i+1} , respectively. We collect per-pixel ratios on valid pixels

$$\mathcal{R}_{ij}^t = \left\{ \frac{\hat{D}_t^i(\mathbf{u})}{\hat{D}_t^{i+1}(\mathbf{u})} \mid \mathbf{u} \in \Omega, \hat{D}_t^i(\mathbf{u}), \hat{D}_t^{i+1}(\mathbf{u}) \in [\epsilon, d_{\max}] \right\}, \quad (2)$$

where Ω denotes pixels satisfying valid depth constraints in both frames. The relative scale ratio for edge $(i, i+1)$ is computed as the robust median:

$$r_{i,i+1} = \operatorname{median}(\mathcal{R}_{i,i+1}), \quad (3)$$

with invalid edges defaulting to $r_{i,i+1} = 1.0$. Since scale factors are inherently positive ($s_i > 0$) and multiplicative in nature, direct optimization in linear space risks negative or zero scales and poorly handles the multiplicative relationships between relative scales. We therefore transform them to log-space where scale factors become additive:

$$x_i = \ln(s_i), \quad \rho_{i,i+1} = \ln(r_{i,i+1}), \quad (4)$$

where x_i is the log-scale of submap \mathcal{S}_i and $\rho_{i,i+1}$ is the log-relative scale constraint between adjacent submaps. This transformation ensures positivity via $s_i = \exp(x_i)$, converts multiplicative scale relationships into additive ones (since $\ln(s_i/s_j) = x_i - x_j$), and yields a convex least-squares problem with improved numerical stability.

We solve for log-scales $\mathbf{x} = [x_1, \dots, x_M]^\top$ by minimizing a regularized least squares objective combining relative consistency and prior regularization:

$$\mathbf{x}^* = \arg \min_{\mathbf{x}} \sum_{(i,j) \in \mathcal{E}} w_{ij} (x_i - x_j - \rho_{ij})^2 + \lambda \sum_{i=1}^M (x_i - \ln s_i^{(0)})^2, \quad (5)$$

where \mathcal{E} denotes edges between overlapping submaps, w_{ij} is the confidence weight for edge (i, j) based on overlap quality, and λ controls the strength of regularization toward the initial log-scale priors $\ln s_i^{(0)}$. This formulation enforces that adjacent submaps respect observed relative scales while preventing deviation from reliable initial estimates.

We solve this nonlinear least squares problem using the Levenberg-Marquardt algorithm, initialized with $x_i^{(0)} = \text{median}(\{\ln s_j^{(0)}\})$ for numerical stability. The final optimized scales are obtained by $s_i^* = \exp(x_i^*)$.

3.2 Depth Reprojection

After obtaining the refined scale factors, we compute the globally-aligned depth maps for all keyframes:

$$D_{k_t}^{\text{aligned}}(\mathbf{u}) = s_m^* \cdot \hat{D}_{k_t}^m(\mathbf{u}), \quad \forall I_{k_t} \in \mathcal{S}_m, \forall \mathbf{u} \in \Omega. \quad (6)$$

We then fuse these aligned depth maps into an initial SDF volume $\mathcal{V}_{\text{initial}}$ using volumetric fusion with running average. The fusion aggregates multi-view depth observations into a coherent 3D scene representation, reducing per-frame noise while preserving geometric details. For each keyframe I_{k_t} , we render a depth map $D_{k_t}^{\text{refined}}$ by first extracting mesh $\mathcal{M}_{\text{initial}}$ from the volume using marching cubes, then render new depth maps from the mesh using off-the-shelf renderer:

$$D_{k_t}^{\text{refined}}(\mathbf{u}) = \text{render}(\mathcal{M}_{\text{initial}}, \mathbf{K}, \mathbf{T}_{k_t}, \mathbf{u}). \quad (7)$$

This projection yields a set of ‘‘clean’’ depth maps that show strong geometric and scale consistency enforced by the global volumetric representation, exhibiting reduced noise, fewer outliers, and are particularly helpful in improving multi-view coherence in outdoor scenes as we will show in our ablation studies. These refined depth maps, together with their corresponding keyframes \mathcal{I}' , serve as inputs to our VFM-augmented neural reconstruction pipeline described next.

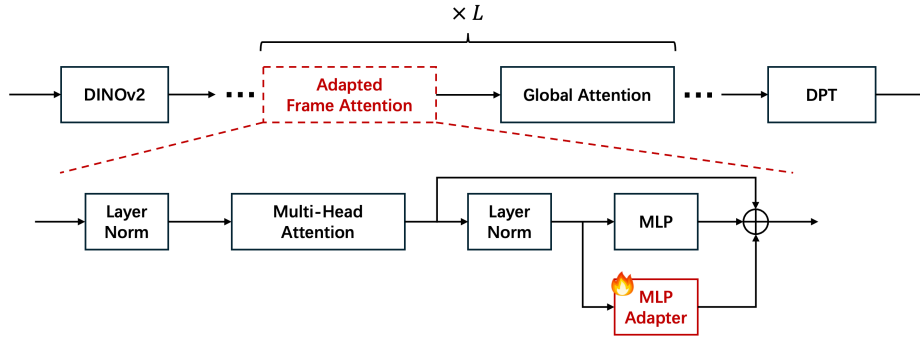


Fig. 3: Network Architecture. Details of our adapted VGGT for VFM-augmented volumetric reconstruction network, in which only the MLP adapter is trainable.

3.3 VFM-augmented Neural Reconstruction

Even after scale alignment (§3.1) and depth reprojection (§3.2), the refined depth maps $D_{k_t}^{\text{refined}}$ inevitably contain residual artifacts stemming from prediction uncertainty and minor geometric inconsistencies. When integrated into an initial SDF volume $\mathcal{V}_{\text{initial}}$, such imperfections can lead to small spurious components (“floaters”) and locally inconsistent surfaces.

To mitigate these artifacts, we employ established neural reconstruction methods to process the noisy SDF and produce a refined implicit representation [32]. Different from standard pipelines that rely solely on ImageNet-pretrained CNN features, we augment the 2D feature extractor with transferable VFM features from VGGT, improving cross-domain generalization while preserving the strong inductive biases of CNN encoders.

Feature Extraction and Fusion Given input keyframes $\mathcal{I} = \{I_{k_t}\}_{t=1}^P$ and refined depth maps $\mathcal{D} = \{D_{k_t}^{\text{refined}}\}_{t=1}^P$, we first extract VFM features $\mathcal{F}_{k_t}^{\text{vggt}} \in \mathbb{R}^{C_v \times H_v \times W_v}$ combined from intermediate layers of the VGGT encoder with a DPT head, alongside CNN features $\mathcal{F}_{k_t}^{\text{cnn}} \in \mathbb{R}^{C_c \times H_c \times W_c}$ via a CNN encoder.

To adapt the VGGT features for our reconstruction task while preserving the pre-trained representation, we opt for parameter efficient finetuning and employ a lightweight MLP adapter [47]. As shown in Figure 3, the adapter is plugged into the transformer block of the VGGT encoder, right after the multi-head attention, enabling effective fine-tuning of the feature distribution while keeping the foundation model frozen. We only insert adapters to the frame attention layers as we empirically found out that adapting only frame-attention transformer blocks yields better results than also adapting global-attention blocks, therefore we adopt this setting in all experiments.

The adapted VGGT features are resized to match the spatial dimensions of the CNN image features, and then fused via element-wise summation. We then back-project the aggregated 2D features into a 3D volume using known camera

parameters, averaging across views to construct the enhanced feature volume:

$$\mathcal{F}_{\text{vol}}(\mathbf{x}_v) = \frac{1}{\sum_{t=1}^P w_{t,v}} \sum_{t=1}^P w_{t,v} \mathcal{F}_{k_t}^{\text{comb}}(\mathbf{u}_{t,v}), \quad (8)$$

where $\mathcal{F}^{\text{comb}}$ is the fused VFM and CNN features, $w_{t,v} = \mathbb{1}_{[\mathbf{x}_v \in \text{frustum}_{k_t}]}$ indicates voxel visibility, and $\mathbf{u}_{t,v} = \pi(\mathbf{K}\mathbf{T}_{k_t}^{-1}\tilde{\mathbf{x}}_v)$ denotes the projected image coordinates with bilinear interpolation. This augmented feature volume, concatenated with the initial SDF reconstruction from the previous section, is processed by a 3D U-Net decoder:

$$\mathcal{V}_{\text{refined}} = F_{\theta}^{\text{dec}}([\mathcal{F}_{\text{vol}}, \mathcal{V}_{\text{initial}}]), \quad (9)$$

where $[\cdot, \cdot]$ denotes channel-wise concatenation and F_{θ}^{dec} represents a multi-level 3D convolutional decoder.

In addition to the volumetric features, we also incorporate point back-projection features from [32]. For every 3D query point, we back-project the image features from the corresponding 2D location and aggregate multi-view features through average pooling. These point back-projection features are concatenated with $\mathcal{V}_{\text{refined}}$ to form a hybrid representation that combines both volumetric and point-wise information. The concatenated features are then processed through two separate MLPs to predict the signed distance field and occupancy probability, respectively.

Neural Reconstruction We train the reconstruction network on keyframes paired with ground-truth SDF fragments \tilde{S} . The training data are prepared following the pipeline provided in [32].

The full network is trained to minimize the following total reconstruction loss:

$$\mathcal{L}_{\text{total}} = \mathcal{L}_{\text{sdf}} + \mathcal{L}_{\text{occ}}. \quad (10)$$

We apply binary cross-entropy loss on the predicted occupancy $\hat{o}(\mathbf{x})$ to distinguish between occupied and free space:

$$\mathcal{L}_{\text{occ}} = \text{BCE}(\hat{o}(\mathbf{x}), o(\mathbf{x})), \quad \forall \mathbf{x} \in \mathcal{X}_{\text{occ}}^{\text{valid}}, \quad (11)$$

where $o(\mathbf{x}) \in \{0, 1\}$ denotes the ground-truth occupancy derived from the ground-truth SDF map, and $\mathcal{X}_{\text{occ}}^{\text{valid}}$ represents the set of valid query points.

We also enforce consistency between the predicted SDF values and the ground-truth SDF at observed surface points.

$$\mathcal{L}_{\text{sdf}} = \frac{1}{|\mathcal{X}_{\text{sdf}}|} \sum_{\mathbf{x} \in \mathcal{X}_{\text{sdf}}} \|t(\hat{\phi}(\mathbf{x})) - t(\phi_{\text{gt}}(\mathbf{x}))\|_1, \quad (12)$$

where $\hat{\phi}(\mathbf{x}) = \tanh(\hat{\phi}_{\text{logits}}(\mathbf{x}))$ denotes the SDF logits which are transformed via tanh to obtain normalized signed distance values, \mathcal{X}_{sdf} denotes the set of voxels where ground-truth occupancy $o(\mathbf{x}) > 0.5$. The log transform is defined as $t(x) = \text{sign}(x) \cdot \ln(|x| + 1)$. Note that the SDF loss is only computed when $|\mathcal{X}_{\text{sdf}}| > 0$.

4 Experiments

4.1 Datasets, Baselines, and Metrics

Datasets. We follow the standard protocol in neural volumetric reconstruction [32, 36, 57] and use ScanNet [6] as our primary training and evaluation dataset. ScanNet is a large-scale indoor RGB-D dataset comprising 1,613 room-scale scans across 807 indoor scenes. We train our VFM-Recon on the official training split and report results on all 100 scans from the official test split.

To assess cross-domain generalizability, we follow Zuo *et al.* [58] and evaluate on two additional out-of-distribution datasets: TUM RGB-D [35], and Tanks and Temples [18]. Compared to ScanNet, TUM RGB-D consists of more constrained sequences and exhibits distinct motion and viewpoint statistics, often featuring inward-facing trajectories with close-range observations; Tanks and Temples includes large-scale scenes spanning not only indoor spaces but also outdoor environments, with substantially higher appearance, geometry, and scale variability. Notably, while Zuo *et al.* [58] only reported qualitative results on a single Tanks and Temples scene, we perform both qualitative and quantitative evaluation across all available training scenes in the dataset.

Baselines. We aim to provide a comprehensive evaluation by comparing our VFM-Recon against a broad spectrum of neural reconstruction methods, ranging from earlier approaches such as VoRTX [34] and NeuralRecon [36] to more recent SoTA systems including GP-Recon [57] and GeoRecon [42]. For cross-domain evaluation, since most of the latest methods do not release code, we adopt NeuralRecon [36], SimpleRecon [30], and FineRecon [32] as representative baselines and run their official implementations on both datasets under the same input setting. Beyond neural reconstruction models, we additionally include two geometry-aware VFMs, VGGT [38] and MoGe-2 [40], to better contextualize our performance and highlight the benefits of reconciling foundation priors with scale consistent volumetric reconstruction.

Metrics. We follow the standard evaluation protocol in neural reconstruction [30, 32, 36, 57]. For reconstructed meshes, we report 3D metrics including Accuracy (*Acc.*), Completeness (*Comp.*), Chamfer distance (*Cham.*), Precision (*Prec.*), Recall, and F1 score (*F1*). For rendered depth, we additionally report 2D metrics: Absolute Relative error (*Abs.Rel.*), Absolute Difference (*Abs.Diff.*), Squared Relative error (*Sq.Rel.*), Completion (*Comp.*), and threshold accuracies ($\delta < 1.05$, $\delta < 1.25$), where the δ metrics denote the percentage of pixels whose predicted depth is within a multiplicative threshold of the ground truth.

4.2 Implementation Details

For scale alignment, we construct each submap from $n = 8$ consecutive keyframes with an overlap of $o = 4$ frames, except on ScanNet where we use a longer window of $n = 16$. For depth reprojection, the globally aligned depth maps are fused via running-average volumetric fusion at a voxel resolution of 0.04m. For VFM-augmented neural reconstruction, we employ a bottleneck MLP adapter with

Table 1: Quantitative Evaluation of Reconstructed Mesh on ScanNet [6]. The best result is marked in **bold**, the second best is underlined, and the third is in *italic*.

Method	Venues	Acc.↓	Comp.↓	Cham.↓	Prec.↑	Recall↑	F1↑
VoRTX [34]	3DV’21	5.4	9.0	-	70.8	58.8	64.1
NeuralRecon [36]	CVPR’21	5.4	12.8	-	68.4	47.9	56.2
SimpleRecon [30]	ECCV’22	6.1	<i>5.5</i>	5.8	68.6	<i>65.8</i>	67.1
FineRecon [32]	ICCV’23	5.6	<u>5.4</u>	<i>5.5</i>	<u>76.9</u>	<u>71.3</u>	<u>73.6</u>
DG-Recon [16]	ICCV’23	3.9	6.8	<u>5.4</u>	<u>76.9</u>	63.6	<i>69.4</i>
Zuo <i>et al.</i> [58]	RA-L’23	5.8	11.0	-	66.5	50.5	57.2
AirPlanes [43]	CVPR’24	<i>4.9</i>	6.0	<u>5.4</u>	70.8	62.2	66.2
PanoRecon [46]	CVPR’24	6.4	8.9	-	65.6	53.0	58.4
GeoRecon [42]	RA-L’25	5.6	9.8	7.7	68.3	53.0	59.5
GP-Recon [57]	TVCG’25	3.9	9.3	6.6	77.6	61.0	68.1
DetailRefine [4]	ICRA’25	<u>4.4</u>	9.3	6.9	70.9	54.1	61.3
VFM-Recon (Ours)	-	5.6	4.7	5.1	<i>75.7</i>	73.2	74.3

Table 2: Quantitative Evaluation of Rendered Depth on ScanNet [6]. The best result is marked in **bold**, the second best is underlined, and the third is in *italic*.

Method	Venues	Abs.Rel.↓	Abs.Diff.↓	Sq.Rel.↓	$\delta < 1.05\uparrow$	$\delta < 1.25\uparrow$	Comp.↑
VoRTX [34]	3DV’21	6.1	9.4	3.7	<i>79.0</i>	95.0	96.1
NeuralRecon [36]	CVPR’21	6.5	10.6	3.1	-	94.8	90.9
SimpleRecon [30]	ECCV’22	4.3	8.9	1.3	70.2	98.1	-
FineRecon [32]	ICCV’23	5.5	8.5	3.8	<u>82.8</u>	<u>95.8</u>	<u>97.2</u>
DG-Recon [16]	ICCV’23	6.2	9.9	4.0	-	93.7	<i>96.6</i>
Zuo <i>et al.</i> [58]	RA-L’23	5.2	<i>8.7</i>	<i>2.5</i>	-	94.8	90.6
GeoRecon [42]	RA-L’25	5.6	9.0	3.1	-	94.0	92.9
GP-Recon [57]	TVCG’25	<u>4.5</u>	7.7	<u>2.2</u>	-	<i>95.4</i>	-
VFM-Recon (Ours)	-	<i>5.0</i>	<u>8.1</u>	3.7	85.5	96.8	97.5

dimensions $1024 \rightarrow 512 \rightarrow 1024$. The point CNN and voxel CNN share the same FPN-style design [23] with an EfficientNetV2-S backbone [37] but are trained independently, while the 3D CNN follows a U-Net architecture. We optimize the model with Adam [17] using batch size 2, an initial learning rate of 1×10^{-3} , and a decay factor of 0.1. All experiments are conducted on two NVIDIA A6000 GPUs with 48GB memory each, and training takes approximately one week.

4.3 Results and Discussion

In-domain Evaluations. The quantitative results on reconstructed meshes and rendered depth are reported in Table 1 and Table 2. Overall, VFM-Recon achieves the best performance on most metrics, ranking second on *Abs.Diff.* and third on *Prec.* and *Abs.Rel.*, demonstrating consistent gains on in-domain data.

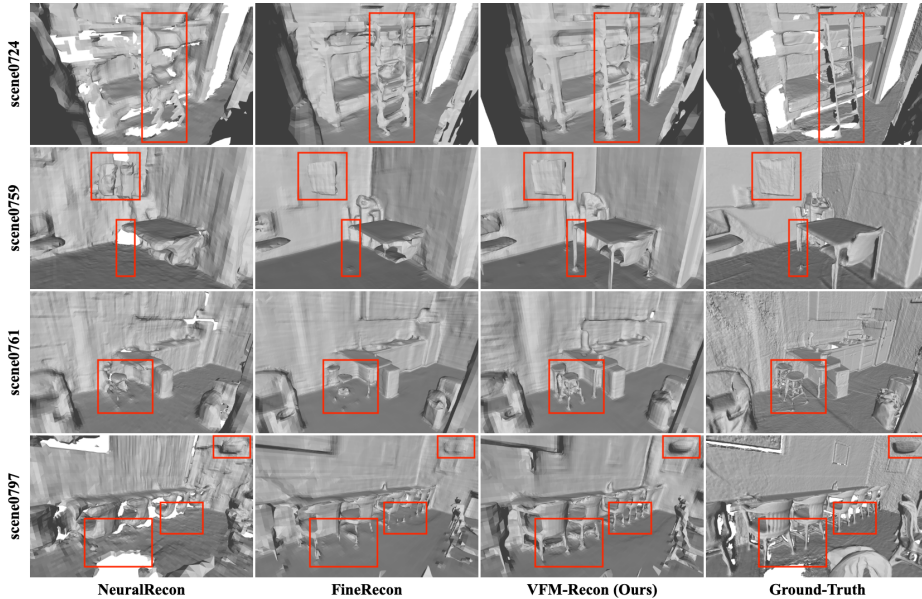


Fig. 4: Qualitative Comparison on ScanNet [6]. Compared with NeuralRecon [36] and FineRecon [32], our VFM-Recon reconstructs better structure details like staircases, chair/tables legs, and TV surfaces, as highlighted in the red bounding boxes.

However, we do observe relatively weaker results on *Acc.* and *Sq.Rel.*, as both metrics are particularly sensitive to a small number of outliers. *Acc.* averages the distance from reconstructed surface points to the closest ground-truth surface; we argue that it is more affected by minor spurious fragments or slight surface thickening in fine-detail regions, which can arise as a by-product of improving coverage and completeness. *Sq.Rel.* squares the depth residual and normalizes it by the ground-truth depth, thereby amplifying a few large outliers (e.g., from close-range or far-depth pixels); as a result, it could decrease even when overall threshold accuracy improves.

Furthermore, the qualitative comparisons of reconstructed mesh are provided in Figure 4. It can be observed that our VFM-Recon better preserves fine-grained geometric details than NeuralRecon [36] and FineRecon [32], including the staircase structures in *scene0724*, the thin supporting structures in *scene0759/0761/0797*, and planar surfaces in *scene0759*. Surprisingly, in several challenging regions such as long table legs in *scene0759/0761*, our reconstructions are even visually cleaner and more complete than the officially provided ScanNet pseudo ground truth, which is generated by BundleFusion [7] with post-processing. Overall, these examples confirm the improved reconstruction capability of our proposed VFM-Recon.

Cross-domain Evaluations. The quantitative comparisons on reconstructed mesh are summarized in Table 3. Overall, Our VFM-Recon achieves the best per-

Table 3: Cross-Domain Evaluation of Reconstructed Mesh. The best result is marked in **bold**, the second best is underlined, and the third is in *italic*.

Method	Venues	TUM RGBD [35]			Tanks&Temples [18]		
		Prec.↑	Recall↑	F1↑	Prec.↑	Recall↑	F1↑
VoRTX [34]	3DV’21	28.0	19.4	22.9	-	-	-
NeuralRecon [36]	CVPR’21	49.4	24.8	32.4	42.6	24.7	30.2
SimpleRecon [30]	ECCV’22	40.0	<u>48.0</u>	<u>43.5</u>	44.4	<i>31.5</i>	<i>35.7</i>
Zuo <i>et al.</i> [58]	RAL’23	36.9	13.3	19.5	-	-	-
FineRecon [32]	ICCV’23	27.4	32.2	29.6	<i>47.0</i>	26.5	33.1
GP-Recon [57]	TVCG’25	<u>48.9</u>	32.8	<i>38.6</i>	-	-	-
VGGT [38]	CVPR’25	25.2	19.9	21.9	<u>51.0</u>	<u>55.8</u>	<u>51.8</u>
MoGe-2 [40]	NeurIPS’25	27.3	<i>33.5</i>	29.9	41.7	39.2	40.3
VFM-Recon (Ours)	-	<i>43.6</i>	50.7	46.7	68.6	73.7	70.1

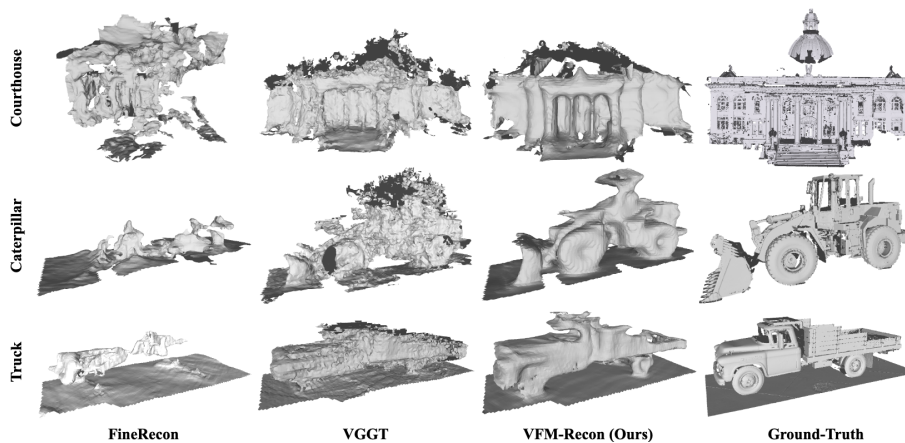


Fig. 5: Qualitative Comparison on Tanks and Temples [18]. Compared with FineRecon [32] and VGGT [38], our VFM-Recon reconstructs more complete structures with fewer fragmented artifacts across challenging outdoor scenes.

formance across almost all metrics on both datasets. Especially, on the most challenging Tanks and Temples [18], VFM-Recon consistently outperforms representative feed-forward neural reconstruction baselines and also surpasses geometry-aware VFMs [38, 40], and obtain the most pronounced improvements in *Recall* and *F1* (*73.7* vs. *55.8* and *70.1* vs. *51.8*), indicating substantially better surface coverage and overall reconstruction quality. These results validate that enforcing scale-consistent geometric alignment and integrating VFM priors into volumetric reconstruction enable robust cross-domain transfer.

Moreover, the representative reconstructions on Tanks and Temples are visualized in Figure 5. FineRecon [32] suffers from severe incompleteness under domain shift, producing fragmented surfaces and missing large portions of the scene

Table 4: Ablation Studies. V.D. denotes the use of VGGT depth, S.A. and D.R refer to our scale alignment and depth reprojection step respectively, A.V. indicates task-adapted VGGT features.

Variant	Settings				ScanNet [6]			Tanks&Temples [18]		
	V.D.	S.A.	D.R.	A.V.	Prec.↑	Recall↑	F1↑	Prec.↑	Recall↑	F1↑
Default	✓	✓	✓	✓	<u>75.7</u>	<u>73.2</u>	<u>74.3</u>	68.6	73.7	70.1
w/o S.A.	✓		✓	✓	74.5	71.5	72.8	45.5	<u>48.4</u>	45.4
w/o D.R.	✓	✓		✓	76.5	75.4	75.8	<u>59.8</u>	48.3	<u>50.5</u>
w/o S.A.&D.R.	✓			✓	73.7	71.0	72.3	49.0	32.6	36.0
Adapted VGGT Only				✓	<u>75.7</u>	72.2	73.9	42.8	31.6	33.7
Naive VGGT Only					73.5	70.8	72.1	42.5	31.7	33.4

structure. In contrast, while VGGT [38] yields geometrically plausible shapes, its reconstructions tend to be noisy and less scale consistent, leading to over-fragmented geometry and distorted thin structures. Our VFM-Recon, however, reconstructs substantially more complete and coherent surfaces, preserving the global shape layout and structural details with fewer spurious floaters, like the facade structure in *Courthouse* and the characteristic silhouettes in *Caterpillar* and *Truck*. These qualitative observations are consistent with the quantitative gains, and highlight that enforcing scale consistency is critical for transferring foundation priors to robust cross-domain mesh reconstruction.

4.4 Ablation Study

To validate our design choices, we ablate the key components of VFM-Recon in Table 4. Overall, removing any component degrades performance (see *w/o S.A.*, *w/o S.A.&D.R.*, *Adapted VGGT Only*, and *Naive VGGT Only*), confirming that the proposed modules contribute complementary benefits. Interestingly, solely removing depth reprojection (the *w/o D.R.* row) slightly improves in-domain results on ScanNet [6] but causes a much larger degradation under domain shift. This indicates that depth reprojection provides stronger cross-domain regularization by enforcing multi-view consistency in a geometry-grounded manner. We believe this is a reasonable trade-off: depth reprojection may introduce quantization error that might be harmful for in-domain data, yet substantially improves robustness when the depth prior becomes less reliable.

5 Conclusion

We presented **VFM-Recon**, a novel framework that bridges between transferable VFM priors and the scale consistency required by neural volumetric reconstruction. Our key insight is to decouple cross-domain reconstruction into two complementary stages: (i) a lightweight geometric alignment module that resolves the scale ambiguity and inter-frame inconsistency of foundation depth

predictions, enabling stable multi-view fusion, and (ii) a VFM-augmented neural reconstruction pipeline that integrates task-adapted foundation features to improve robustness under domain shift. Extensive experiments on in-domain as well as cross-domain evaluations demonstrate that VFM-Recon achieves SoTA performance, with particularly strong gains on challenging cross-domain outdoor scenes. We believe VFM-Recon offers a practical and general recipe for leveraging foundation priors in scene-level reconstruction, opening up new opportunities for robust 3D perception across diverse environments.

References

1. Boss, M., Huang, Z., Vasishtha, A., Jampani, V.: Sf3d: Stable fast 3d mesh reconstruction with uv-unwrapping and illumination disentanglement. In: 2025 IEEE/CVF Conference on Computer Vision and Pattern Recognition (CVPR). pp. 16240–16250 (2025). <https://doi.org/10.1109/CVPR52734.2025.01514>
2. Božić, A., Palafox, P., Thies, J., Dai, A., Nießner, M.: Transformerfusion: monocular rgb scene reconstruction using transformers. In: Proceedings of the 35th International Conference on Neural Information Processing Systems. NIPS '21, Curran Associates Inc., Red Hook, NY, USA (2021)
3. Cabon, Y., Stoffl, L., Antsfeld, L., Csurka, G., Chidlovskii, B., Revaud, J., Leroy, V.: Must3r: Multi-view network for stereo 3d reconstruction. In: 2025 IEEE/CVF Conference on Computer Vision and Pattern Recognition (CVPR). pp. 1050–1060 (2025). <https://doi.org/10.1109/CVPR52734.2025.00106>
4. Chu, F., Cong, Y., Chen, R.: Detailrefine: Towards fine-grained and efficient online monocular 3d reconstruction. In: 2025 IEEE International Conference on Robotics and Automation (ICRA). pp. 15783–15790 (2025). <https://doi.org/10.1109/ICRA55743.2025.11128107>
5. Chu, F., Cong, Y., Wang, Y., Chen, R.: Detailrecon: Focusing on detailed regions for online monocular 3d reconstruction. *IEEE Transactions on Multimedia* **27**, 3266–3278 (2025). <https://doi.org/10.1109/TMM.2025.3535311>
6. Dai, A., Chang, A.X., Savva, M., Halber, M., Funkhouser, T., Nießner, M.: Scannet: Richly-annotated 3d reconstructions of indoor scenes. In: 2017 IEEE Conference on Computer Vision and Pattern Recognition (CVPR). pp. 2432–2443 (2017). <https://doi.org/10.1109/CVPR.2017.261>
7. Dai, A., Nießner, M., Zollhöfer, M., Izadi, S., Theobalt, C.: Bundlefusion: Real-time globally consistent 3d reconstruction using on-the-fly surface reintegration. *ACM Trans. Graph.* **36**(3) (May 2017). <https://doi.org/10.1145/3054739>
8. Danier, D., Aygün, M., Li, C., Bilen, H., Mac Aodha, O.: Depthcues: Evaluating monocular depth perception in large vision models. In: 2025 IEEE/CVF Conference on Computer Vision and Pattern Recognition (CVPR). pp. 20049–20059 (2025). <https://doi.org/10.1109/CVPR52734.2025.01867>
9. DeTone, D., Malisiewicz, T., Rabinovich, A.: Superpoint: Self-supervised interest point detection and description. In: Proceedings of the IEEE conference on computer vision and pattern recognition workshops. pp. 224–236 (2018)
10. Duisterhof, B.P., Zust, L., Weinzaepfel, P., Leroy, V., Cabon, Y., Revaud, J.: Mast3r-sfm: A fully-integrated solution for unconstrained structure-from-motion. In: 2025 International Conference on 3D Vision (3DV). pp. 1–10 (2025). <https://doi.org/10.1109/3DV66043.2025.00008>

11. Duzceker, A., Galliani, S., Vogel, C., Speciale, P., Dusmanu, M., Pollefeys, M.: Deepvideomvs: Multi-view stereo on video with recurrent spatio-temporal fusion. In: Proceedings of the IEEE/CVF Conference on Computer Vision and Pattern Recognition. pp. 15324–15333 (2021)
12. Feng, Z., Yang, L., Guo, P., Li, B.: Cvrecon: Rethinking 3d geometric feature learning for neural reconstruction. In: 2023 IEEE/CVF International Conference on Computer Vision (ICCV). pp. 17704–17714 (2023). <https://doi.org/10.1109/ICCV51070.2023.01627>
13. Hong, Y., Zhang, K., Gu, J., Bi, S., Zhou, Y., Liu, D., Liu, F., Sunkavalli, K., Bui, T., Tan, H.: LRM: Large reconstruction model for single image to 3d. In: The Twelfth International Conference on Learning Representations (2024), <https://openreview.net/forum?id=s11U8vvsFF>
14. Hu, M., Yin, W., Zhang, C., Cai, Z., Long, X., Chen, H., Wang, K., Yu, G., Shen, C., Shen, S.: Metric3d v2: A versatile monocular geometric foundation model for zero-shot metric depth and surface normal estimation. *IEEE Transactions on Pattern Analysis and Machine Intelligence* **46**(12), 10579–10596 (2024). <https://doi.org/10.1109/TPAMI.2024.3444912>
15. Huang, J., Artemov, A., Chen, Y., Zhi, S., Xu, K., Nießner, M.: Ssr-2d: Semantic 3d scene reconstruction from 2d images. *IEEE Transactions on Pattern Analysis and Machine Intelligence* **46**(12), 8486–8501 (2024). <https://doi.org/10.1109/TPAMI.2024.3410032>
16. Ju, J., Tseng, C.W., Bailo, O., Dikov, G., Ghafoorian, M.: Dg-recon: Depth-guided neural 3d scene reconstruction. In: 2023 IEEE/CVF International Conference on Computer Vision (ICCV). pp. 18138–18148 (2023). <https://doi.org/10.1109/ICCV51070.2023.01667>
17. Kingma, D.P., Ba, J.: Adam: A method for stochastic optimization. In: 3rd International Conference on Learning Representations, ICLR 2015, San Diego, CA, USA, May 7-9, 2015, Conference Track Proceedings (2015), <http://arxiv.org/abs/1412.6980>
18. Knapitsch, A., Park, J., Zhou, Q.Y., Koltun, V.: Tanks and temples: benchmarking large-scale scene reconstruction. *ACM Trans. Graph.* **36**(4) (Jul 2017). <https://doi.org/10.1145/3072959.3073599>
19. Leroy, V., Cabon, Y., Revaud, J.: Grounding image matching in 3d with mast3r. In: Computer Vision – ECCV 2024: 18th European Conference, Milan, Italy, September 29–October 4, 2024, Proceedings, Part LXXII. p. 71–91. Springer-Verlag, Berlin, Heidelberg (2024). https://doi.org/10.1007/978-3-031-73220-1_5
20. Li, W., Liu, S., Qiao, P., Dou, Y.: Mono3r: Exploiting monocular cues for geometric 3d reconstruction. In: Proceedings of the 33rd ACM International Conference on Multimedia. p. 11081–11090. MM '25, Association for Computing Machinery, New York, NY, USA (2025). <https://doi.org/10.1145/3746027.3755722>
21. Lilova, V., Chakravorty, T., Bibo, J.I., Boccaletti, E., Li, B., Baxová, L., Snoek, C.G.M., Salehi, M.: Evaluating foundation models’ 3d understanding through multi-view correspondence analysis. In: UniReps: 3rd Edition of the Workshop on Unifying Representations in Neural Models (2025), <https://openreview.net/forum?id=Gx55orCXfu>
22. Lin, H., Chen, S., Liew, J.H., Chen, D.Y., Li, Z., Zhao, Y., Peng, S., Guo, H., Zhou, X., Shi, G., Feng, J., Kang, B.: Depth anything 3: Recovering the visual space from any views. In: The Fourteenth International Conference on Learning Representations (2026), <https://openreview.net/forum?id=yirunib818>

23. Lin, T.Y., Dollár, P., Girshick, R., He, K., Hariharan, B., Belongie, S.: Feature pyramid networks for object detection. In: 2017 IEEE Conference on Computer Vision and Pattern Recognition (CVPR). pp. 936–944 (2017). <https://doi.org/10.1109/CVPR.2017.106>
24. Lindenberger, P., Sarlin, P.E., Pollefeys, M.: Lightglue: Local feature matching at light speed. In: Proceedings of the IEEE/CVF international conference on computer vision. pp. 17627–17638 (2023)
25. Maggio, D.R., Lim, H., Carlone, L.: VGGT-SLAM: Dense RGB SLAM optimized on the $SL(4)$ manifold. In: The Thirty-ninth Annual Conference on Neural Information Processing Systems (2025), <https://openreview.net/forum?id=631jkCGMhE>
26. Murai, R., Dexheimer, E., Davison, A.J.: Mast3r-slam: Real-time dense slam with 3d reconstruction priors. In: 2025 IEEE/CVF Conference on Computer Vision and Pattern Recognition (CVPR). pp. 16695–16705 (2025). <https://doi.org/10.1109/CVPR52734.2025.01556>
27. Murez, Z., van As, T., Bartolozzi, J., Sinha, A., Badrinarayanan, V., Rabinovich, A.: Atlas: End-to-end 3d scene reconstruction from posed images. In: Computer Vision – ECCV 2020: 16th European Conference, Glasgow, UK, August 23–28, 2020, Proceedings, Part VII. p. 414–431. Springer-Verlag, Berlin, Heidelberg (2020). https://doi.org/10.1007/978-3-030-58571-6_25
28. Newcombe, R.A., Izadi, S., Hilliges, O., Molyneaux, D., Kim, D., Davison, A.J., Kohi, P., Shotton, J., Hodges, S., Fitzgibbon, A.: Kinectfusion: Real-time dense surface mapping and tracking. In: 2011 10th IEEE International Symposium on Mixed and Augmented Reality. pp. 127–136 (2011). <https://doi.org/10.1109/ISMAR.2011.6092378>
29. Sayed, M., Aleotti, F., Watson, J., Qureshi, Z., Garcia-Hernando, G., Brostow, G., Vicente, S., Firman, M.: Doubletake: Geometry guided depth estimation. In: Computer Vision – ECCV 2024: 18th European Conference, Milan, Italy, September 29–October 4, 2024, Proceedings, Part LXXIII. p. 121–138. Springer-Verlag, Berlin, Heidelberg (2024). https://doi.org/10.1007/978-3-031-73464-9_8
30. Sayed, M., Gibson, J., Watson, J., Prisacariu, V., Firman, M., Godard, C.: Simplercon: 3d reconstruction without 3d convolutions. In: Computer Vision – ECCV 2022: 17th European Conference, Tel Aviv, Israel, October 23–27, 2022, Proceedings, Part XXXIII. p. 1–19. Springer-Verlag, Berlin, Heidelberg (2022). https://doi.org/10.1007/978-3-031-19827-4_1
31. Shi, J., Zhi, S., Xu, K.: Planerectr++: Unified query learning for joint 3d planar reconstruction and pose estimation. *IEEE Transactions on Pattern Analysis and Machine Intelligence* **48**(1), 962–981 (2026). <https://doi.org/10.1109/TPAMI.2025.3610500>
32. Stier, N., Ranjan, A., Colburn, A., Yan, Y., Yang, L., Ma, F., Angles, B.: Finerecon: Depth-aware feed-forward network for detailed 3d reconstruction. In: 2023 IEEE/CVF International Conference on Computer Vision (ICCV). pp. 18377–18386 (2023). <https://doi.org/10.1109/ICCV51070.2023.01689>
33. Stier, N., Rich, A., Sen, P., Höllerer, T.: Anigrad: Anisotropic gradient-adaptive sampling for 3d reconstruction from monocular video. In: 2025 IEEE/CVF Conference on Computer Vision and Pattern Recognition (CVPR). pp. 21814–21823 (2025). <https://doi.org/10.1109/CVPR52734.2025.02032>
34. Stier, N., Rich, A., Sen, P., Höllerer, T.: Vortex: Volumetric 3d reconstruction with transformers for voxelwise view selection and fusion. In: 2021 International Conference on 3D Vision (3DV). pp. 320–330 (2021). <https://doi.org/10.1109/3DV53792.2021.00042>

35. Sturm, J., Engelhard, N., Endres, F., Burgard, W., Cremers, D.: A benchmark for the evaluation of rgb-d slam systems. In: 2012 IEEE/RSJ International Conference on Intelligent Robots and Systems. pp. 573–580 (2012). <https://doi.org/10.1109/IROS.2012.6385773>
36. Sun, J., Xie, Y., Chen, L., Zhou, X., Bao, H.: Neuralrecon: Real-time coherent 3d reconstruction from monocular video. In: 2021 IEEE/CVF Conference on Computer Vision and Pattern Recognition (CVPR). pp. 15593–15602 (2021). <https://doi.org/10.1109/CVPR46437.2021.01534>
37. Tan, M., Le, Q.: Efficientnetv2: Smaller models and faster training. In: Proceedings of the 38th International Conference on Machine Learning. Proceedings of Machine Learning Research, vol. 139, pp. 10096–10106. PMLR (18–24 Jul 2021), <https://proceedings.mlr.press/v139/tan21a.html>
38. Wang, J., Chen, M., Karaev, N., Vedaldi, A., Rupprecht, C., Novotny, D.: Vggt: Visual geometry grounded transformer. In: 2025 IEEE/CVF Conference on Computer Vision and Pattern Recognition (CVPR). pp. 5294–5306 (2025). <https://doi.org/10.1109/CVPR52734.2025.00499>
39. Wang, R., Xu, S., Dai, C., Xiang, J., Deng, Y., Tong, X., Yang, J.: Moge: Unlocking accurate monocular geometry estimation for open-domain images with optimal training supervision. In: 2025 IEEE/CVF Conference on Computer Vision and Pattern Recognition (CVPR). pp. 5261–5271 (2025). <https://doi.org/10.1109/CVPR52734.2025.00496>
40. Wang, R., Xu, S., Dong, Y., Deng, Y., Xiang, J., Lv, Z., Sun, G., Tong, X., Yang, J.: Moge-2: Accurate monocular geometry with metric scale and sharp details. In: The Thirty-ninth Annual Conference on Neural Information Processing Systems (2025), <https://openreview.net/forum?id=16mDq7m20K>
41. Wang, S., Leroy, V., Cabon, Y., Chidlovskii, B., Revaud, J.: Dust3r: Geometric 3d vision made easy. In: 2024 IEEE/CVF Conference on Computer Vision and Pattern Recognition (CVPR). pp. 20697–20709 (2024). <https://doi.org/10.1109/CVPR52733.2024.01956>
42. Wang, Y., Chu, F., Han, Z., Tang, Y.: Georecon: Geometric coherence for online 3d scene reconstruction from monocular video. *IEEE Robotics and Automation Letters* **10**(1), 500–507 (2025). <https://doi.org/10.1109/LRA.2024.3511423>
43. Watson, J., Aleotti, F., Sayed, M., Qureshi, Z., Aodha, O.M., Brostow, G., Firman, M., Vicente, S.: Airplanes: Accurate plane estimation via 3d-consistent embeddings. In: 2024 IEEE/CVF Conference on Computer Vision and Pattern Recognition (CVPR). pp. 5270–5280 (2024). <https://doi.org/10.1109/CVPR52733.2024.00504>
44. Weinzaepfel, P., Leroy, V., Lucas, T., Brégier, R., Cabon, Y., ARORA, V., Antsfeld, L., Chidlovskii, B., Csurka, G., Revaud, J.: Croco: Self-supervised pre-training for 3d vision tasks by cross-view completion. In: *Advances in Neural Information Processing Systems* (2022), <https://openreview.net/forum?id=wZefHUM5ri>
45. Weinzaepfel, P., Lucas, T., Leroy, V., Cabon, Y., Arora, V., Brégier, R., Csurka, G., Antsfeld, L., Chidlovskii, B., Revaud, J.: Croco v2: Improved cross-view completion pre-training for stereo matching and optical flow. In: 2023 IEEE/CVF International Conference on Computer Vision (ICCV). pp. 17923–17934 (2023). <https://doi.org/10.1109/ICCV51070.2023.01647>
46. Wu, D., Yan, Z., Zha, H.: Panorecon: Real-time panoptic 3d reconstruction from monocular video. In: 2024 IEEE/CVF Conference on Computer Vision and Pattern Recognition (CVPR). pp. 21507–21518 (2024). <https://doi.org/10.1109/CVPR52733.2024.02032>

47. Xu, L., Xie, H., Qin, S.Z.J., Tao, X., Wang, F.L.: Parameter-efficient fine-tuning methods for pretrained language models: A critical review and assessment (2023), <https://arxiv.org/abs/2312.12148>
48. Yang, L., Kang, B., Huang, Z., Xu, X., Feng, J., Zhao, H.: Depth anything: Unleashing the power of large-scale unlabeled data. In: 2024 IEEE/CVF Conference on Computer Vision and Pattern Recognition (CVPR). pp. 10371–10381 (2024). <https://doi.org/10.1109/CVPR52733.2024.00987>
49. Yang, L., Kang, B., Huang, Z., Zhao, Z., Xu, X., Feng, J., Zhao, H.: Depth anything v2. In: The Thirty-eighth Annual Conference on Neural Information Processing Systems (2024), <https://openreview.net/forum?id=cFTi3gLJ1X>
50. Yang, X., Ming, Y., Cui, Z., Calway, A.: Fd-slam: 3-d reconstruction using features and dense matching. In: 2022 International Conference on Robotics and Automation (ICRA). pp. 8040–8046 (2022). <https://doi.org/10.1109/ICRA46639.2022.9812049>
51. Ye, H., Liu, Y., Liu, Y., Shen, S.: Neuralplane: Structured 3d reconstruction in planar primitives with neural fields. In: The Thirteenth International Conference on Learning Representations (2025), <https://openreview.net/forum?id=5UKrnKuspb>
52. Yin, W., Zhang, C., Chen, H., Cai, Z., Yu, G., Wang, K., Chen, X., Shen, C.: Metric3d: Towards zero-shot metric 3d prediction from a single image. In: 2023 IEEE/CVF International Conference on Computer Vision (ICCV). pp. 9009–9019 (2023). <https://doi.org/10.1109/ICCV51070.2023.00830>
53. Zeng, Z., Wu, Y., Park, H., Wang, D., Yang, F., Soatto, S., Lao, D., Hong, B.W., Wong, A.: RSA: Resolving scale ambiguities in monocular depth estimators through language descriptions. In: The Thirty-eighth Annual Conference on Neural Information Processing Systems (2024), <https://openreview.net/forum?id=vH7GcaDhAo>
54. Zhang, C., Song, H., Wei, Y., Yu, C., Lu, J., Tang, Y.: GeoLRM: Geometry-aware large reconstruction model for high-quality 3d gaussian generation. In: The Thirty-eighth Annual Conference on Neural Information Processing Systems (2024), <https://openreview.net/forum?id=eM5d7ZmekA>
55. Zheng, D., Huang, S., Li, Y., Wang, L.: Learning from videos for 3d world: Enhancing MLLMs with 3d vision geometry priors. In: The Thirty-ninth Annual Conference on Neural Information Processing Systems (2025), <https://openreview.net/forum?id=oUYmk8WaG0>
56. Zhou, Z., Ma, Y., Fan, J., Zhang, S., Jing, F., Tan, M.: Eprecon: An efficient framework for real-time panoptic 3d reconstruction from monocular video. In: 2025 IEEE International Conference on Robotics and Automation (ICRA). pp. 2026–2033 (2025). <https://doi.org/10.1109/ICRA55743.2025.11128258>
57. Zou, Z.X., Huang, S.S., Cao, Y.P., Mu, T.J., Shan, Y., Fu, H., Zhang, S.H.: Gp-recon: Online monocular neural 3d reconstruction with geometric prior. IEEE Transactions on Visualization and Computer Graphics **31**(9), 4790–4804 (2025). <https://doi.org/10.1109/TVCG.2024.3413860>
58. Zuo, X., Yang, N., Merrill, N., Xu, B., Leutenegger, S.: Incremental dense reconstruction from monocular video with guided sparse feature volume fusion. IEEE Robotics and Automation Letters **8**(6), 3876–3883 (2023). <https://doi.org/10.1109/LRA.2023.3273509>